Identifying the Distribution of Al^{3+} in LiNi$_{0.8}$Co$_{0.15}$Al$_{0.05}$O$_2$

Nicole M. Trease,[†] Ieuan D. Seymour,[†] Maxwell D. Radin,[‡] Haodong Liu,[§] Hao Liu,[∥] Sunny Hy,[§] Natalya Chernova,[⊥] Pritesh Parikh,[§] Arun Devaraj,[#] Kamila M. Wiaderek,[∥] Peter J. Chupas,[∥] Karena W. Chapman,[∥] M. Stanley Whittingham,[⊥] Ying Shirley Meng,*[,§] Anton Van der Van,[‡] and Clare P. Grey*[,†]

[†]Department of Chemistry, University of Cambridge, Lensfield Road, Cambridge, CB2 1EW, U.K.

[‡]Materials Department, University of California, Santa Barbara, Santa Barbara, California 93106, United States

[§]Department of NanoEngineering, University of California, San Diego, La Jolla, California 92093, United States

[∥]X-ray Division, Advanced Photon Source, Argonne National Laboratory, Argonne, Illinois 60439, United States

[⊥]Institute for Materials Research, SUNY Binghamton, Binghamton, New York 13902-6000, United States

[#]Physical and Computational Sciences Directorate, Pacific Northwest National Laboratory, Richland, Washington 99352, United States

ⓢ *Supporting Information*

ABSTRACT: The doping of Al into layered Li transition metal (TM) oxide cathode materials, LiTMO$_2$, is known to improve the structural and thermal stability, although the origin of the enhanced properties is not well understood. The effect of aluminum doping on layer stabilization has been investigated using a combination of techniques to measure the aluminum distribution in layered LiNi$_{0.8}$Co$_{0.15}$Al$_{0.05}$O$_2$ (NCA) over multiple length scales with ^{27}Al and ^{7}Li MAS NMR, local electrode atom probe (APT) tomography, X-ray and neutron diffraction, DFT, and SQUID magnetic susceptibility measurements. APT ion maps show a homogeneous distribution of Ni, Co, Al, and O$_2$ throughout the structure at the single particle level in agreement with the high-temperature phase diagram. ^{7}Li and ^{27}Al NMR indicates that the Ni^{3+} ions undergo a dynamic Jahn−Teller (JT) distortion. ^{27}Al NMR spectra indicate that the Al reduces the strain associated with the JT distortion, by preferential electronic ordering of the JT lengthened bonds directed toward the Al^{3+} ion. The ability to understand the complex atomic and orbital ordering around Al^{3+} demonstrated in the current method will be useful for studying the local environment of Al^{3+} in a range of transition metal oxide battery materials.
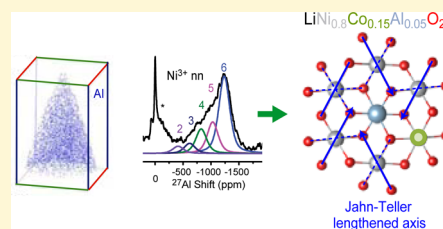
■ INTRODUCTION

Layered Ni rich mixed transition metal oxides have generated significant interest as lower cost and higher capacity Li ion battery cathode materials to replace LiCoO$_2$.[1] Layered LiNiO$_2$ ($R\bar{3}m$) was originally studied as a potential cathode material; however, it was found that stoichiometric LiNiO$_2$ could not be synthesized as a result of the tendency of Ni^{3+} to reduce to Ni^{2+}.[2] The presence of Ni^{2+} in the Li layers was found to hinder Li migration.[3] LiNiO$_2$ was also found to have poor thermal stability in the delithiated state causing safety concerns for functional commercialization.[4] The structure of LiNiO$_2$ has been debated due to the complex orbital ordering found for Ni^{3+}.[5] Ni^{3+} occupy octahedral sites in the structure of LiNiO$_2$ and have a low spin d^7 (t$_{2g}^6$e$_g^{*1}$) configuration.[4−6] EXAFS studies identified that each Ni^{3+} undergoes a positive Jahn−Teller (JT) distortion in which two of the Ni−O bonds are elongated and four shortened.[4] Unlike in other compounds, such as NaNiO$_2$[7] and LiMnO$_2$,[8,9] a cooperative ordering of the JT distortions is not observed in LiNiO$_2$. The lack of a cooperative ordering has been suggested in a number of studies to be due to a dynamic JT process, in which the distortion on each Ni^{3+} center fluctuates due to thermal vibrations.[4,6,10,11]

EPR studies of LiNiO$_2$ observed a dynamic JT distortion and only showed static behavior below 30 K.[6] For delithiated Li$_x$NiO$_2$, there is a transformation from a dynamic to a static JT distortion as a result of the coupling between the Li vacancy ordering and the JT distortion on the Ni^{3+} centers that leads to a cooperatively distorted monoclinic cell.[4]

Doping of other cations into the parent LiNiO$_2$ structure has led to increased thermal stability, stabilization of the layered structure, and improved electrochemical performance. One of the most widely studied Ni-rich materials, LiNi$_{0.8}$Co$_{0.15}$Al$_{0.05}$O$_2$, which will be referred to as NCA, has even been commercialized. NCA adopts the same ($R\bar{3}m$) layered structure as LiNiO$_2$, in which Co^{3+} and Al^{3+} are substituted for Ni^{3+} in octahedral sites. The substitution of Co^{3+} was found to stabilize the layered structure and improve the electrochemical performance in LiNi$_{1−y}$Co$_y$O$_2$,[12] although other studies suggest that Co^{3+} may lead to a strained TM layer. TM with different ionic radii have different M−O bond lengths causing a strain of the

edge sharing MO_6 octahedra. In Al-doped $LiNi_{0.45}Mn_{0.45}Co_{1-y}Al_yO_2$ (NMC), it has been suggested that the doping of Al reduces this strain due to its smaller ionic radii leading to a more ordered TM structure.[13,14]

Even though it is electrochemically inactive, the substitution of Al^{3+} in the structure has been found to improve the thermal stability and capacity retention even at low doping levels (5%).[15] Although the addition of Al^{3+} is essential in order to improve the thermal stability of NCA, the exact mechanism of stabilization or ordering of Al within the TM layer is not fully understood. It was proposed by Guilmard et al.[16,17] that the enhanced thermal stability was due to the stability of Al^{3+} tetrahedral sites within the structure that hinders the migration of Ni^{3+} required to transform the structure from the layered ($R\bar{3}m$) to a spinel-like structure. In a series of $Li_{1+x}(Ni_{0.40}Mn_{0.40}Co_{0.2-z}Al_z)_{1-x}O_2$, it was found that by increasing the Al^{3+} content and decreasing the amount of unstable Ni^{4+} and Co^{4+} formed in the delithiated state, an increased thermal stability was observed.[18] For $LiNi_{1/3}Mn_{1/3}Co_{1/3-z}Al_zO_2$ it was found that the structural stability imparted by Al was sensitive to how Al^{3+} was distributed in the structure.[19,20] Samples in which the Al^{3+} was distributed homogeneously throughout the material were found to be less reactive in the presence of electrolyte. It has also been observed in $LiNi_{1-y}Al_yO_2$ there is a tendency for Ni and Al segregation into nanodomains.[21] Developing techniques that probe the local structure and distribution of Al within the structure of NCA is therefore essential in order to understand the role that Al plays in enhancing the structural stability.

Proper characterization of the transition metal (TM) layer is required to understand the mechanisms of increased performance and to further the development of new materials with increased capacity. There are many methods employed to investigate the structure of layered metal oxides. Neutron and X-ray techniques provide a detailed analysis of long-range order. TEM provides a measure of local order but is only a surface sensitive technique. Recently, APT (atom probe tomography) has been used to probe the cation distribution in layered materials.[22] This technique employs a large (~kV) DC bias and a pulsed UV laser to induce field evaporation of ions from a sample prepared in the form of a needle. A position sensitive detector and time-of-flight measurements enable identification of atomic positions at the nanoscale coupled with chemical composition, providing unparalleled three-dimensional (3D) maps of the system under investigation. They were able to identify Li-rich and Li-poor regions in Li-excess $Li_{1.2}Ni_{0.2}Mn_{0.6}O_2$.

The application of $^{6/7}Li$ solid state NMR to the study of lithium batteries has been fundamental to the study of the changes in the local structure as a function of charge in batteries.[23−32] The diamagnetic NMR shift region of Li is extremely narrow (0 ± 5 ppm). Although Li is a quadrupolar nucleus (^7Li $I = 1/2$ and ^6Li $I = 1$), it has a small quadrupole moment and typically does not experience a large quadrupolar broadening compared to other quadrupolar nuclei. In paramagnetic materials, the unpaired electrons on the TM lead to the Fermi contact shift that can shift resonances thousands of ppm and to a paramagnetic broadening of the spectrum due to the electron−nuclear dipolar coupling. The assignment of the $^{6/7}Li$ NMR shift near paramagnetic centers has mainly been the focus of NMR studies on battery materials to date.[23,29,31,33,34] Although NMR of other nuclei has been performed to investigate changes in local structure by observing the transition

metals, such as ^{27}Al and ^{59}Co in dilute Ni^{3+} structures[24−28] and ^{51}V in vanadium phosphates,[23] sulfides,[35] and oxides.[23,36−39]

The development of $^{6/7}Li$ NMR as a probe of the Li local structure near paramagnetic TMs, specifically in layered metal oxides, has been based primarily on two methods: experimental NMR of materials with dilute TM concentration and assignment using DFT calculations, the later being limited until recent years due to the computational expense of calculations. Marichal et al. observed the static and MAS $^{6/7}Li$ NMR shift in a series of $LiNi_{1-y}Co_yO_2$ for increasing Ni content.[31] Although the high Ni content structures gave broad resonances, they developed a correlation between the isotropic NMR shift and Ni^{3+} content. It was observed that the isotropic shift was dependent on the number of Ni^{3+} neighbors. Further experimental and computational work by Carlier[33] and the groups of Grey and Delmas developed a direct correlation between the orbital overlap of the M−O−Li bonds to the NMR shift that followed the Goodenough-Kanamori rules.[23,33] In dilute paramagnetic samples, they showed that the contribution to the NMR shift was additive, and the total shift was a sum of contributions from all the 90° and 180° M−O−Li nearest neighbors. Only nuclei within the first metal coordination sphere contribute to the overall shift due to the orbital overlap with the paramagnetic center (M) with Li through a M−O−Li bond.

Although the NMR shift for ^6Li and ^7Li is identical for the same Li environment, many of the previous Li NMR studies have been performed using the ^6Li isotope, even though it is only 7.5% naturally abundant (N.A.) compared to ^7Li (92.5% N.A.) requiring isotopic enrichment or long experiment times to signal average. ^6Li has the advantage of having a smaller quadrupole moment and a smaller gyromagnetic ratio than ^7Li. The greater advantage comes from the smaller gyromagnetic ratio ($\gamma(^6Li)/\gamma(^7Li) = 0.38$) which leads to greater Hz/ppm resolution in the frequency domain allowing the isotropic peaks to be sufficiently separated from each other and spinning sidebands. With recent developments of fast MAS (magic-angle spinning) NMR techniques to obtain isotropic spectra, such as aMAT[29] or pj-MATPASS,[40] high-resolution ^7Li NMR spectra of paramagnetically broadened materials is now achievable in a reduced experimental time with greater signal-to-noise compared to ^6Li.

Recently, Middlemiss et al.[34] applied a spin-flipping approach on an optimized structure of $LiNiO_2$ with a collinear JT distortion to calculate the individual DFT bond pathway contributions to the $^{6/7}Li$ Fermi-contact (FC) NMR shift. This method confirmed the additive nature of the FC shift observed experimentally. In layered materials, the nearest neighbor M (M_{nn}) atoms interact with the Li through two ~90° M−O−Li bond pathways, and the next nearest neighbors (M_{nnn}) interact with the Li with one ~180° M−O−Li bond pathway as depicted in Figure 1, leading to bond pathway contribution to the NMR shift of $\delta_{nn,i}$ and $\delta_{nnn,i}$, respectively. Each M−O−Li bond pathway contribution is proportional to the difference in the unpaired spin density at the Li site when the M spins are aligned ferromagnetically and when one is flipped, i.e. ferrimagnetic. The 4 different M environments in Figure 1 lead to 4 different shift contributions for the Li^+ in the $LiNiO_2$ structure. There are two M_{nn} environments, one contains 2 short Ni−O bonds and the other contains a long and short Ni−O bond with a shift contribution of δ_{SS} and δ_{SL}, respectively, where the subscript denotes each Ni−O bond. The two M_{nnn} environments only have contributions from one Ni−O bond:
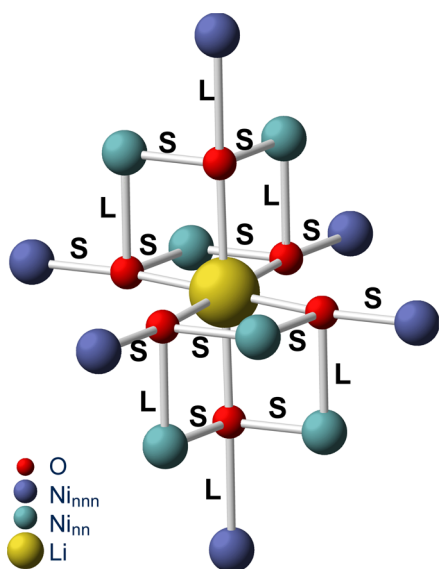
Figure 1. Local structure around a Li atom in a Jahn−Teller distorted layered $LiNiO_2$. S and L represent JT short and long bonds, respectively. Blue and purple atoms represent Ni_{nn} and Ni_{nnn}, respectively.

one short and one long with shift contributions of δ_S and δ_L, respectively. The overall FC shift, δ_{FC}, is a sum of all the individual bond pathways between the observed NMR nucleus and each M, $\delta_{FC} = \Sigma(\delta_{nn,i} + \delta_{nnn,i})$. It was found that the shifts predicted with hybrid DFT calculations were sensitive to the amount of Hartree−Fock exchange in the hybrid functional, with most experimental values falling within the range of values calculated with 20 to 35% HF exchange.[34,41] Their calculated ^7Li shift contributions using the B3LYP functional with 20% HF exchange are $\delta_{SS} = 6.9$, $\delta_{SL} = -29.6$, $\delta_S = 44.4$, and $\delta_L = 325.6$.[34] They also assigned the observed experimental shift in dilute Ni mixed metal oxides to a dynamic JT distortion. In a dynamic JT structure, the Li nucleus experiences an axially averaged shift during the NMR experiment, $\delta_{nn} = (\delta_{SS} + 2\delta_{SL})/3$ and $\delta_{nnn} = (2\delta_S + \delta_L)/3$ assuming rapid fluctuation of the JT axis on the NMR time scale.[34] For $LiNiO_2$, their calculated axially averaged contributions to the shift are $\delta_{nn,dJT} = -17.4$ ppm and $\delta_{nnn,dJT} = 138.1$ ppm, yielding an overall shift of 724 ppm, which agreed well with reported experimental values.[34]

^{27}Al NMR is very sensitive to the Al local environment and its coordination, and it has been readily used in the study of materials; but only a few studies have been reported on battery materials.[24−28] ^{27}Al is also a quadrupolar nucleus ($I = 5/2$) but has a larger quadrupole moment than ^6Li or ^7Li and can experience a large quadrupolar shift and broadening. In diamagnetic materials, octahedral AlO_6 environments are observed near 0 ppm, whereas tetrahedral AlO_4 environments are observed near 70 ppm. Previously, only one study reported ^{27}Al NMR of Al-doped into the transition metal layer of a paramagnetic material. In this study, a very broad Al signal was observed for delithiated Al-doped $LiNiO_2$.[25] Based upon the NMR shifts of diamagnetic Al, they observed that increased levels of Al doping (greater than 20%) resulted in the observation of pseudotetrahedral Al. Just prior to the submission of this manuscript, Dogan et al.[42] analyzed the ^6Li and ^{27}Al NMR spectra of NCA and NMC (Li-$Ni_xMn_yCo_{1−x−y}O_2$) with varying Al content. They found that

increasing Al content above 5% in NCA led to the presence of diamagnetic peaks indicating aluminate phase segregation.

In nonparamagnetic materials, ^{27}Al NMR has also been used to study the structure in $LiAl_xCo_{1−x}O_2$.[24,28] They found that with increased Co content the Al resonance shifts to greater frequencies, giving shifts that could be incorrectly assigned to tetrahedral environments. This increasing shift was ascribed to a +7 ppm shift per Co neighbor. The use of ^{27}Al NMR has also been applied to study the effectiveness of coating on layered battery materials, such as Al_2O_3 coated $LiCoO_2$[26] and AlF_3 coated $Li[Li_{1/9}Ni_{1/3}Mn_{5/9}]O_2$.[27] In all the previous ^{27}Al NMR studies of layered oxide materials, the spectra of high Ni^{3+} content with Al in the bulk material have yet to be assigned or analyzed.

Here we have developed a method of using ^{27}Al NMR as a probe of the local structure in high Ni content Al-doped $LiNiO_2$ paramagnetic materials using DFT NMR shift calculations. We also show that APT provides a method to determine the bulk distribution of ions within a material. By combining ^{27}Al and ^7Li NMR, SQUID magnetic susceptibility measurements, APT, neutron and X-ray diffraction coupled with first-principles structural and NMR shift calculations we show that the Al distribution is homogeneous throughout the bulk material in the dynamic JT distorted layered NCA.

EXPERIMENTAL METHODS

Materials. $Li[Ni_{0.8}Co_{0.15}Al_{0.05}]O_2$ was used as purchased (NAT1050, TODA America).

NMR. ^{27}Al MAS (magic-angle spinning) NMR spectra were acquired on a Bruker Avance II (4.7 T) and a Bruker Avance III (7 T) using a Bruker 1.3 mm MAS probe. A Hahn-echo pulse sequence with $\pi/2 = 1.5$ μs optimized on solid AlF_3 was used. Solid AlF_3 was used as a secondary reference at −17 ppm (with respect to aqueous $Al(NO_3)_3$ at 0 ppm).[27]

^7Li MAS NMR spectra were acquired on a Bruker Avance II (4.7 T) using a Bruker 1.3 mm MAS probe. Spectra were referenced to solid Li_2CO_3 at 0 ppm using a $\pi/2 = 1.02$ μs. The pj-MATPASS sequence[40] was used to obtain the isotropic ^7Li spectrum.

Neutron and X-ray Diffraction. Time of flight (TOF) powder neutron diffraction data was collected on the POWGEN instrument at the Spallation Neutron Source (SNS) in the Oak Ridge National Lab (ORNL). Around 3 g of powder was filled into a vanadium sample can and sent via the mail-in service to the SNS. Data were collected at a wavelength of 1.066 Å to cover a d-spacing range of 0.3−3.0 Å.

Synchrotron X-ray powder diffraction was taken at the Advanced Photon Source (APS) at Argonne National Laboratory (ANL) on beamline 11-BM ($\lambda = 0.45999$ Å). The beamline uses a sagittally focused X-ray beam with a high precision diffractometer circle and perfect Si(111) crystal analyzer detection for high sensitivity and resolution.

Full pattern joint X-ray and neutron Rietveld refinement was performed to extract the structure parameters using GSAS software with EXPGUI interface.[43,44]

Atom Probe Tomography (APT). Samples were prepared using the FEI Helios focused ion beam at Pacific Northwest National Laboratory, from pristine powders scattered onto a Si substrate. A pick and place technique was used to affix particles onto a Si microtip array followed by Pt deposition to protect the particle from Ga ions during the milling process. Subsequently an annular mill with Ga ions gave the final needle shaped specimen. The needle specimens were then analyzed using a CAMECA LEAP 4000 XHR APT system at Pacific Northwest National Laboratory.

The fabrication procedure and preparation conditions are provided in detail in the Supporting Information.

SQUID Magnetic Susceptibility. The temperature dependence of the dc magnetization was measured using a Quantum Design SQUID

magnetometer (MPMS XL-5) on cooling the samples from 350 to 2 K in a magnetic field of 1000 Oe.

Structure Optimization and Phase Diagram Calculations. DFT calculations to find optimized structures were performed with the Vienna ab initio Simulation Package (VASP)[45−48] with the on-site Coulomb correction of Dudarev et al.[49] (DFT + U) and PAW pseudopotentials.[50,51] These DFT calculations were used to parametrize cluster expansions using the Clusters Approach to Statistical Mechanics (CASM) code.[52−55] The effect of vibrational contributions to the free energy on the relative stability of γ-LiAlO$_2$ and the layered phases was accounted for using the method of ref 56. Additional calculation details can be found in the Supporting Information.

First Principle Calculations of NMR Shifts. Calculations of the ^{27}Al hyperfine shifts were done using methods described previously.[29,34,41,57] Periodic spin polarized DFT calculations were performed in CRYSTAL.[58] Previous studies[34,41,59] have shown that the use of hybrid functionals in the DFT description of the electronic structure is necessary to get an accurate description of hyperfine shifts, and, furthermore, the spin transfer mechanism is sensitive to the amount of Hartree−Fock exchange included in the functionals construction. We therefore adopt the approach outlined in refs 29, 34, and 41 in which the hyperfine parameters are calculated with two B3LYP[60,61] hybrid functionals containing 20% and 35% Hartree−Fock exchange, which will be referred to as HYB20 and HYB35 respectively.

The extended basis sets (BSII) from ref 41 for Li (TZDP[62]) and O (IGLOIII[63]) were used for the computation of the hyperfine shift parameters. The Ni basis set (Ahlrichs DZP[62]) was taken from ref 34, and the Al set (IGLOIII[63]) was taken from ref 57. The number of Gaussian primitives and the contraction scheme used for each basis set, along with details of the convergence criteria used for the calculations, are provided in the Supporting Information.

The DFT + U optimized Li$_{32}$Ni$_{31}$Al$_1$O$_{64}$ structure was used for all of the hyperfine calculations without further optimization. Single point energy calculations were performed in the ferromagnetic state in order to calculate the unpaired spin density transferred to the Al nuclear position from the neighboring Ni^{3+} centers through an intervening O. The amount of unpaired spin density transferred can be directly related to the Fermi contact shift that would be expected in the zero temperature regime. The zero temperature shift is scaled into the paramagnetic temperature regime under which the NMR experiment is performed. Using the approach in ref 57 the scaling factor, Φ, can be expressed as $B_0 \mu_{eff}^2/3k_b g_e \mu_B S(T-\Theta)$ where B_0 is the applied magnetic field, μ_{eff} is the effective magnetic moment, k_b is Boltzmann's constant, g_e is the free electron g value, μ_B is the Bohr magneton, S is the formal spin of Ni ($S_{Ni3+} = 1/2$), T is the experimental temperature, and Θ is the Weiss constant. The values of μ_{eff} and Θ were taken from the fits to experimental magnetic data, and the NMR temperature was taken as 320 K to account for frictional heating during MAS.

The electron−nuclear dipolar and quadrupolar tensors were also calculated and are given in the Supporting Information along with further details of the calculations.

RESULTS AND DISCUSSION

In order to test the hypothesis that Al is uniformly distributed in NCA, the LiNi$_x$Co$_y$Al$_{1−x−y}$O$_2$ phase diagram was calculated using cluster expansions parametrized by density functional theory (DFT) calculations. These phase diagrams were constructed from the free energy landscape of layered LiNi$_x$Co$_y$Al$_{1−x−y}$O$_2$, as well as the line compound γ-LiAlO$_2$ which is more stable than layered LiAlO$_2$ at high temperatures.[56]

The calculated NCA phase diagram at 1000 K (representative of synthesis temperatures) shows that Al has a high solubility in layered NCA (Figure 2). For Al concentrations in the TM layer below ∼80%, the system consists of a single layered phase. At high Al concentrations (>80%) phase separation occurs, with a two-phase equilibrium between the layered phase and γ-LiAlO$_2$. Additional phase diagrams using
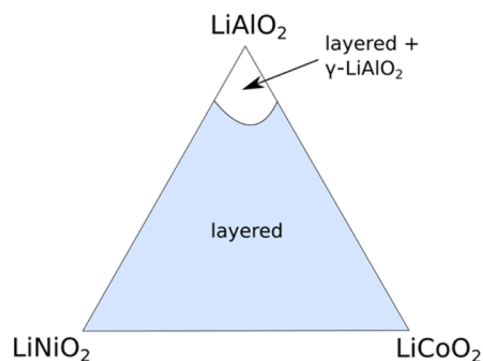

Figure 2. NCA phase diagram calculated at 1000 K using DFT + U with U_{Ni} = 5 eV and U_{Co} = 0 eV.

different values of U on the Ni and Co confirm the high solubility of Al regardless of the choice of U (Figure S1).

The long-range order, structure, and Li/M/O occupancy of NCA was confirmed using both X-ray and neutron diffraction. In this refinement, the occupancy of O was fixed at 2, the occupancy of 3a and 3b sites were fixed at 1, and the content of Ni + Al + Co was constrained to 1. The isotropic atomic displacement parameter (ADP) model was used in this study, with constraints of U_{iso}(Li1) = U_{iso}(Li2) and U_{iso}(Ni1) = U_{iso}(Ni2) = U_{iso}(Al) = U_{iso}(Co). The Li/Ni mixing, Co, Al occupancy, lattice parameters, oxygen coordinates, and ADPs were allowed to be refined. Figure 3 shows the joint Rietveld
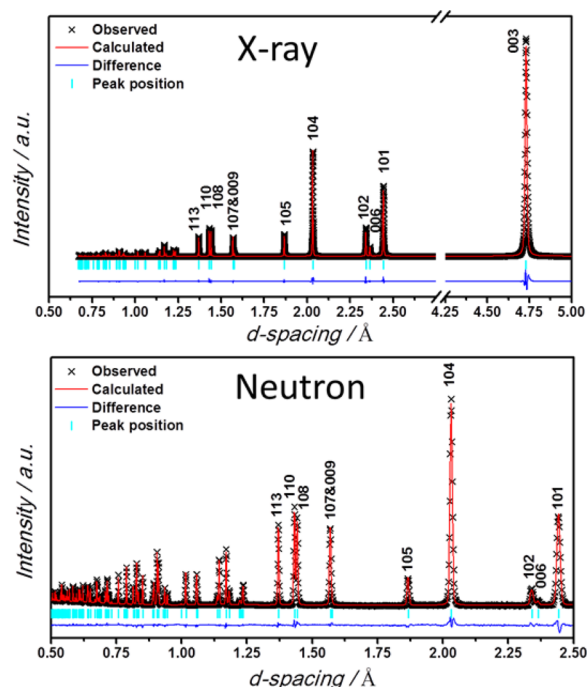

Figure 3. a) X-ray diffraction and b) neutron diffraction patterns of NCA.

refinement of both X-ray and neutron diffraction patterns. All peaks for the NCA sample could be indexed to a single phase with the $R\overline{3}m$ space group.[64,65] The patterns indicate that NCA adopts a well-layered structure with little Li/Ni mixing, 0.1%, as evidenced by the existence of doublets at (006)/(102) and (108)/(110).[66] Table 1 lists the summary of Rietveld refinement results. The refined lattice parameters of NCA are

Table 1. Rietveld Refinement Results[a]

atoms	site	Wyckoff positions			occupancy	$100 \times U_{iso}$
Li1	3a	0	0	0	0.001(1)	1.02(2)
Ni1	3a	0	0	0	0.812(4)	0.262(5)
Co	3a	0	0	0	0.138(4)	0.262(5)
Al	3a	0	0	0	0.050(3)	0.262(5)
Li2	3b	0	0	0.5	0.999(1)	1.02(2)
Ni2	3b	0	0	0.5	0.001(1)	0.262(5)
O	6c	0	0	0.25920(2)	2	0.67(1)

[a]Conventional Rietveld reliability factors: overall R_{wp}: 0.0778.

a = 2.86415(1) Å and c = 14.19052(4) Å. The refined oxygen position of the NCA material is (0, 0, 0.25920(2)). The occupancy of Al has also been refined, which is 5.0(3)%.

The distribution of atoms was measured using APT. APT ion maps provide unique insight into the nanoscale distribution of elements in battery materials. The 3D atom probe maps for Al, Ni, Co, and O_2 maps show a uniform distribution (Figure 4a-e). Maps for Ga, CoO, Ni, O, Ni−Al and Ni−Co are also shown in the Supporting Information (Figures S7 and S8). The presence of Ga arises from the annular milling process to form the needle specimen. The map for Li shows a slightly decreased concentration at the surface, which coincides directly with the Ga enriched region of the needle apex, indicating surface damage due to Ga as the cause for the observed loss of Li near the top surface of the specimen (Figure S7). The mass spectrum shows the peaks assigned for various ions evaporated (Figure 4f). Strong signals for Li, Ni, Co, and O_2 indicate high concentrations of these species. With the exception of Li, the elemental compositions show good agreement with the stoichiometric composition as obtained by neutron diffraction (Table 2). Currently, an effort is underway to study the effect of laser pulse energy on the observed deviation in Li concentration, which will be the subject of a future publication.

Table 2. Bulk Composition Analysis of NCA As Obtained from Neutron Diffraction and Atom Probe Tomography[b]

	Stoichiometric Composition	
	expected from diffraction data (%)	obtained from atom probe tomography[a] (%)
Li	1.000	0.410
Al	0.050	0.058
Ni	0.813	0.800
Co	0.138	0.164
O	2.000	1.825

[a]Average composition determined from three specimens. [b]The Ni composition is taken as the reference. With the exception of Li, the results show a strong agreement.
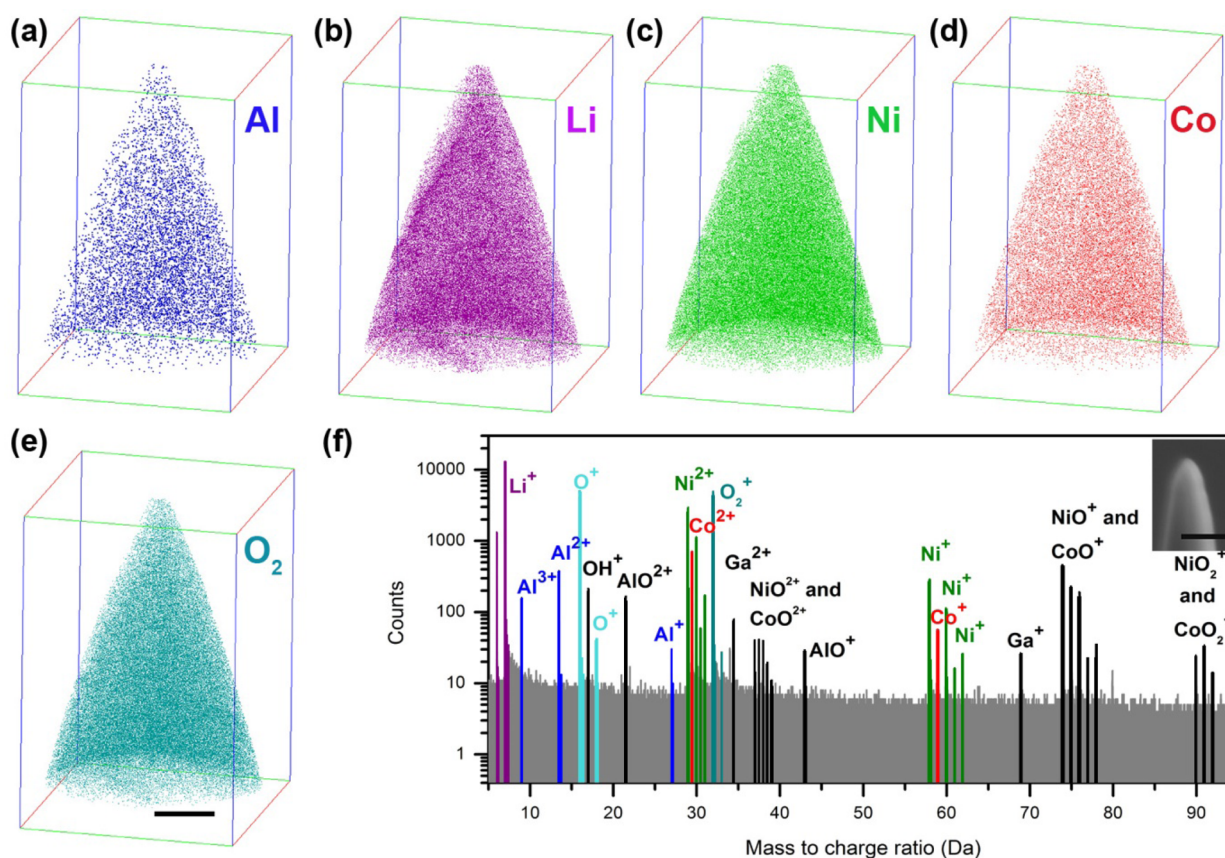

Figure 4. (a-e) Individual atom probe maps for $LiNi_{0.8}Co_{0.15}Al_{0.05}O_2$ (NCA) showing the spatial distribution of Al, Li, Ni, Co, and O_2 ions. The maps clearly show a uniform distribution of the elements. The Al distribution in the pristine powdered sample is uniform and not segregated on grain boundaries as previously believed. (Scale bar is 10 nm.) (f) Mass spectrum for chemical identification of ions present in the analyzed volume. Peaks associated with each ion count are color coded to the respective chemical species. The color coding does not represent the actual mass ranging process followed to identify chemical species. The inset shows the final shape of the sample tip before atom probe tomography. (Scale bar is 300 nm.)

^{7}Li NMR spectra were obtained to probe the local order near the Li. The ^{7}Li NMR Hahn-echo spectra of NCA shown in Figure 5a were acquired at two different spinning speeds, ν_r, of
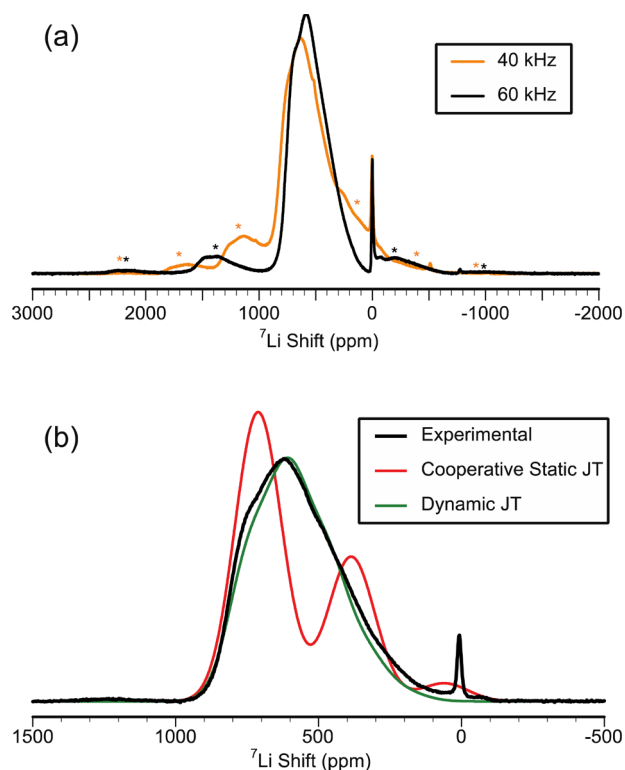

Figure 5. Experimental ^{7}Li NMR spectra of NCA acquired at 7 T. a) Hahn-echo spectra obtained at two different ν_r, 40 kHz (orange) and 60 kHz (black). b) Experimental 1D slices obtained from the 2D pj-MATPASS spectrum (blue) compared to the calculated dynamic JT (red) and static JT (green) spectra. The calculated dynamic JT spectrum indicates a better fit. The peak at 0 ppm is attributed to diamagnetic surface species.

40 and 60 kHz. Even at a low magnetic field of 4.7 T and ν_r of 60 kHz, the electron nuclear dipolar interaction significantly broadens the spectrum, resulting in spinning sidebands overlapping slightly with the isotropic resonances. To accurately assign the shifts, a ^{7}Li pj-MATPASS NMR spectrum was acquired; this 2D NMR sequence suppresses the spinning sidebands, and a 1D spectrum containing only the isotropic resonances is observed (Figure 5b). The full 2D pj-MATPASS spectrum is given in the Supporting Information. This allows accurate deconvolution, fitting, and assignment of the NMR line shape. The sharp resonance at 0 ppm is attributed to diamagnetic impurities on the surface and to Li with 0 Ni^{3+} neighbors, as Al^{3+} and Co^{3+} are both diamagnetic. The broad resonance arises due to the distribution of Li near Ni^{3+} in the layers. As discussed in the Introduction, the Li shift depends not only on the number of Ni^{3+} neighbors in 90° and 180° Li–O–Ni bond pathway configurations but also on the orientation of the JT axis in each of the Li–O–Ni pathways, as JT lengthened and shortened bonds result in different shifts. Using the calculated bond pathway contributions of Middlemiss et al.[34] the shifts of different JT orderings were considered to rationalize the Li spectrum, in which Al, Ni, and Co were assumed to be randomly distributed on the octahedral sites based on the APT results. The static JT (assuming there is a cooperative JT ordering, such as in the $C2/m$ or zigzag

structures) and dynamic JT ^{7}Li NMR spectra were calculated using a random solution model (further details are given in the Supporting Information). The calculated NMR spectra for a static JT distortion give three broad peaks centered at 700, 400, and 50 ppm, whereas the dynamic spectrum has a unique line shape distributed from 1000 to 0 ppm, with the greatest intensity at 724 ppm. Comparison of the calculated spectra with experimental spectra (Figure 5b) indicates there is superb agreement between the experimental and the calculated dynamic JT spectrum. Our analysis of the ^{7}Li NMR spectrum differs slightly from that recently reported by Murakami et al.[67] In their analysis of a NCA spectrum obtained at 14 T, they utilized the correlation of Delmas and co-workers[31] where they assigned three isotropic resonances, two dominant peaks associated with 6 and 5 Ni^{3+} nearest neighbors and another broad peak associated with 1 to 4 Ni^{3+} nearest neighbors. The deviation of intensity of the sites from a random solution model was attributed to Ni-rich and Ni-poor domains. Even though their spectrum was acquired with a very fast spinning speed of 100 kHz, at such a high magnetic field (14 T) the paramagnetic dipolar broadening still caused overlap of the isotropic resonances and spinning sideband manifold making it difficult to identify and quantify the isotropic resonances. Dogan et al.[42] also recently assigned the ^{6}Li NMR spectrum of NCA to two broad resonances attributed to Ni–Co clusters differing from our interpretation. Our results show the importance of accounting for the dynamic JT distortion and using a statistical distribution when assigning $^{6/7}$Li NMR spectra of high Ni content materials.

To further investigate the local structure, ^{27}Al NMR spectra of pristine NCA were obtained at 4.7 T at multiple spinning speeds to determine the isotropic resonances and are given in Figure 6a. The broad signals from −200 to −1500 ppm are the main isotropic resonances; the spinning sidebands are marked with asterisks occurring at multiples of the spinning speed. The isotropic resonances are separated from the spinning sidebands only in the spectrum obtained with a ν_r of 60 kHz at 4.7 T. The sharp resonance at 0 ppm in the ^{27}Al spectra (Figure 6) is attributed to diamagnetic impurities on the surface of the material arising from exposure to air and is less than 0.2% of the material. Thus, greater than 97% of the Al experiences a NMR shift and broadening induced by its proximity to the unpaired electrons on Ni^{3+}, indicating the Al is homogeneously distributed throughout the Ni matrix. This agrees well with the atom probe Al distribution and the high temperature calculated LiNi$_x$Co$_y$Al$_{1-x-y}$O$_2$ phase diagram.

To assign the paramagnetically broadened ^{27}Al NMR shift, DFT calculations were performed on a Li$_{32}$Ni$_{31}$Al$_1$O$_{64}$ super cell, formed by doping an Al atom into an optimized LiNiO$_2$ super cell structure. Further details on generating the super cell are given in the Supporting Information. Contributions to the NMR shift were calculated by using the "spin-flip" procedure using both HYB20 and HYB35 functionals, using $\mu_{eff} = 1.98\ \mu_B$ and $\Theta = 16$ K derived from fits to the magnetic data obtained for NCA. In the Li$_{32}$Ni$_{31}$Al$_1$O$_{64}$ model structure, the Al site has six possible Ni^{3+} nearest neighbors within the transition metal plane with four long JT Ni^{3+}–O bonds orientated toward the Al. The Al is connected to each Ni^{3+} neighbor through two 90° Ni^{3+}–O–Al spin transfer pathways. Thus, the contribution to the Fermi contact shift is only a sum over the nearest neighbor bond pathways, $\delta_{FC} = \Sigma\delta_{nn,i}(90°)$. Three bond pathways from the neighboring Ni^{3+} to the Al are observed in the "zigzag" JT structure (Figure 7). The two P1 (δ_{SS}) pathways consist of two
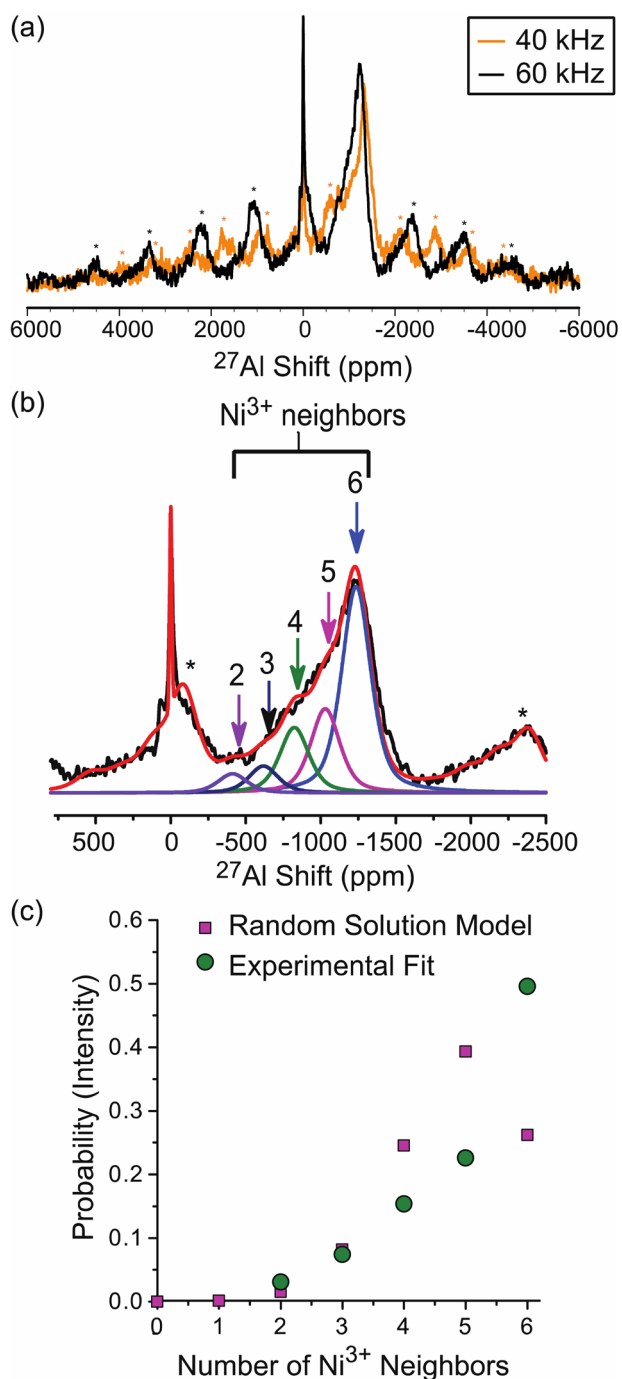
(a)

(b)

(c)

Figure 6. ^{27}Al NMR spectra of NCA acquired at 4.7 T. a) Spectra at two different spinning speeds, ν_r, 40 kHz (orange) and 60 kHz (black). The spinning sidebands are denoted by *. b) Fit (red) of the experimental (black) 60 kHz spectrum using shifts calculated from bond pathways. The individual peaks indicate the number of Ni^{3+} neighbors to Al. c) Comparison of the experimental intensity and the intensity predicted from a random solution model for Al, indicating a preference for Al to be next to Ni. Details of how the random solution model is calculated are given in the Supporting Information.

Al–O–Ni 90° interactions along the short JT axes, and the four P2 (δ_{SL}) pathways consist of two Al–O–Ni interactions, one with a short and the other with a long JT Ni–O bond. Al^{3+} is not JT active, and it behaves as a defect site in the JT distorted matrix, leading to a slight increase and decrease in the length of
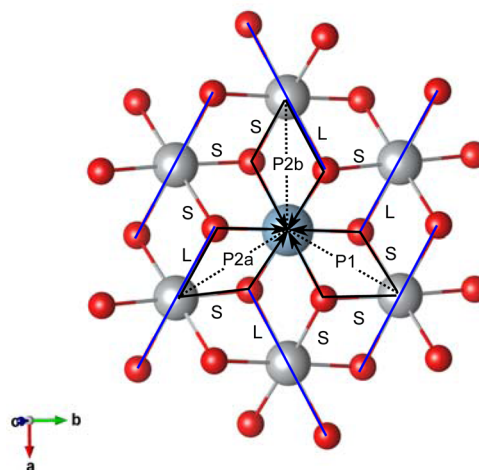

Figure 7. Bond pathway contributions to the Al in the "zigzag" JT distorted layered NCA. (Ni: gray, O: red, Al: light blue, the blue line indicates the JT lengthened axis.)

the JT short and long bonds, respectively, at the Al center. This defect results in the small differences in the bond lengths, splitting the P2 pathway into the P2a and P2b pathways, yielding bond pathway contributions of −339 and −333 ppm, respectively, using the values computed with HYB20. Taking the average of the P2a and P2b pathways, δ_{SL}, the calculated contributions to the shift are $\delta_{SS} = 11$ and $\delta_{SL} = -335$ ppm, giving an axially averaged dynamic JT bond pathway contribution for each Ni^{3+} of $\delta_{nn,dJT} = -220$ ppm for HYB20. A summary of the bond pathway shifts calculated using both HYB20 and HYB35 is shown in Table 3. Although it has been

Table 3. Calculated Bond Pathway Contributions for the Al Center in a "Zigzag" JT Distorted Layered NCA Supercell As Depicted in Figure 4[a]

pathway	^{27}Al NMR shift (ppm)	
	HYB20	HYB35
P1 (δ_{SS})	11	114
P2a	−339	−290
P2b	−333	−254
δ_{SL}	−336	−277
dynamic shift	−220	−143

[a] δ_{SL} is the average of the P2a and P2b pathways.

experimentally observed that each Co^{3+} neighbor will contribute a +7 ppm shift to the ^{27}Al NMR resonance,[24] we have not included this in our model as it is negligible compared to the predicted −220 ppm contribution from Ni^{3+}.

The spectra in Figure 6 were deconvoluted yielding five isotropic resonances attributed to the number of nearest Ni^{3+} neighbors. The experimental shift for Al with 6, 5, 4, 3, and 2 Ni^{3+} neighbors occurs at −1243, −1030, −827, −620, and −413 ppm, respectively, in the ν_r = 60 kHz spectra, and at −1346, −1113, −891, −668, and −445 ppm, respectively, in the ν_r = 40 kHz spectra. Since the overall NMR shift is additive of each of the Ni^{3+}–O–Al pathways, the experimental derived contribution to the dynamic JT NMR shift for each Ni^{3+} is −207 ppm and −223 ppm for ν_r = 60 kHz and 40 kHz, respectively. The difference in the shift obtained at different spinning speeds arises from the dependence of the Fermi-contact shift on the temperature dependent susceptibility.

These values agree exceptionally well with the HYB20 calculated bond pathway contribution of −220 ppm for each Ni^{3+} neighbor.

In Figure 5c, a comparison of the experimental NMR intensity is made with the calculated intensity using a random solution model. Assuming that each experimental peak is associated with Al coordinated by n Ni^{3+}, there are significantly more Al sites with a NMR shift corresponding to 6 Ni^{3+} nearest neighbors (∼40%) than predicted by a random solution model. This would imply that Al has a strong preference to be surrounded by Ni^{3+}, indicative of either Co-deficient nanodomains or strong short-range ordering. Indeed, nanodomains have been observed in high Al content $LiNi_xAl_{1−x}O_2$.[21] EPR studies have indicated that Ni^{3+} experiences a JT stabilization with increasing Al coordination reaching a maximum stabilization with 6 Al neighbors.[6] This stabilization could lead to an increased coordination of Al by Ni. However, the presence of nanodomains is in contrast to the DFT derived high temperature phase diagram (Figure 2) and the homogeneous distribution of all ions observed in the atom probe maps. Furthermore, Monte Carlo calculations based on our cluster expansion predict that there is essentially no short-range ordering of Ni, Co, and Al at synthesis temperatures.

One possible way to reconcile the ^{27}Al NMR spectrum with the cluster expansion and atom-probe results is that the dynamic JT ordering at the Al atom could be quasistatic, i.e., on average more long JT $Ni^{3+}−O$ bonds are orientated toward the Al atom than short bonds. The preference for the JT axis to be directed toward the dopant ions is observed in the DFT optimized structure of $LiNi_{0.5}Co_{0.25}Al_{0.25}O_2$ with a linear ordering of Ni and dopant cations. This linear ordering of cations has also been observed to be more energetically favorable in $LiNi_{0.5}Al_{0.5}O_2$ and $LiNi_{0.5}Co_{0.5}O_2$.[68] In $LiNi_{0.5}Co_{0.25}Al_{0.25}O_2$, each Al is coordinated by 2 Co^{3+} and 4 Ni^{3+} and has four long JT $Ni^{3+}−O$ bonds directed toward it (Figure S2). A pairwise coupling of the JT long bonds on two Ni atoms was predicted to be energetically favorable in $LiNiO_2$ using a spin−orbit model.[5] Assuming a pairwise coupling, an Al coordinated by 5 Ni^{3+} with 4 long and 1 short JT $Ni^{3+}−O$ bonds would only break the coupled distortion on one pair of Ni atoms. An ordering with 3 long and 2 short bonds would break the coupling for two pairs of Ni atoms thus increasing the energy, suggesting that the 4 long and 1 short JT $Ni^{3+}−O$ bond ordering is more energetically favorable. This preferential ordering of the JT long axis toward the Al would increase the dynamic shift experienced by the Al. An Al with only 5 Ni^{3+} neighbors that has on average 4 long and 1 short JT $Ni^{3+}−O$ bonds directed toward it, will have a shift of −1333 ppm similar to that of dynamic 6-Ni^{3+} coordinated Al (−1320 ppm). This would lead to an increase in the expected intensity for 6 Ni^{3+} neighbors in the dynamic JT model. A comparison of the static and dynamic shifts for n = 6, 5, and 4 Ni^{3+} neighbors is given in Table 4 (a full table is available in the Supporting Information). A preferential ordering of the JT long $Ni^{3+}−O$ bond toward the Al atom would increase the expected intensity of NMR resonances associated with n = 6, 5, and 4 Ni^{3+} in agreement with the experimental ^{27}Al NMR spectrum. Our assignment differs from the recent work of Dogan et al.[42] who suggest that there is a preference for Al to have 6 Ni^{3+} neighbors. In their study, they did not take into account the shift dependence of long or short $Ni^{3+}−O$ bonds or assign the dynamic JT shift.

That the shape of the ^{27}Al NMR spectrum is controlled by the energy preference for JT distortions rather than energetic

Table 4. Calculated Dynamic and "Quasistatic" ^{27}Al NMR Shifts for n = 6, 5, and 4 Ni^{3+} Neighbors^a

| | ^{27}Al shifts (HYB20) | | | |
| | JT ordering of $Ni^{3+}−O$ bonds | | | |
no. of Ni^{3+} nn	SL	SS	total shift (ppm)	dynamic shift (ppm)
6	*4*	*2*	−1322	−1320
5	*4*	*1*	−1333	−1100
	3	2	−966	
4	4	0	−1344	−880
	3	*1*	−997	
	2	2	−650	

^{a}The boldface/italic configurations indicate the most probable number of short and long bonds.

preference for chemical ordering can be understood in terms of thermodynamics. The energetic preference for chemical ordering must compete with the thermal energy at synthesis temperatures because ion mobility is low at room temperature. However, the energetic preference for JT orientation need only compete with the room-temperature thermal energy because the reorientation of distortions is facile. Thus, we ascribe the observed ^{27}Al NMR derived distribution to a preference of the JT ordering to be directed toward the Al atom and not a preferential coordination of Al by Ni^{3+}. However, given the limitations of the cluster-expansion model of NCA, we cannot rule out the possibility that some degree of short-range ordering occurs.

CONCLUSIONS

To properly characterize the distribution of Al in doped metal oxides, multiple characterization methods are necessary. The DFT calculated high-temperature phase diagram of $LiNi_xCo_yAl_{1−x−y}O_2$ indicates a single layered phase with Al doping up to 80% in NCA. We have confirmed that NCA adopts a well ordered layered ($R\bar{3}m$) structure with little Li/M layer mixing <0.1% in agreement with the calculated phase diagram. The 3D APT ion maps of elemental distributions allowed us to observe the homogeneous Al distribution at a scale never seen before. Atom probe tomography is an exciting new frontier in understanding the relationship between chemical composition and cycling performance in battery materials.

The combination of DFT structure and NMR shift calculations is essential to assign and interpret paramagnetically broadened NMR spectra. Using the "spin-flip" procedure we have calculated the contribution to the ^{27}Al Fermi-contact NMR shift of an Al coordinated by Ni^{3+}. Both the ^7Li and ^{27}Al NMR indicate that NCA experiences a dynamic JT distortion on the NMR time scale. The distribution of ^{27}Al NMR shifts indicates a preferential ordering of long JT $Ni^{3+}−O$ bonds near the Al^{3+} ion, instead of a preference for Al^{3+} to be coordinated by Ni^{3+}. DFT calculations support that the JT axis has a preferential ordering toward the dopant ions. The local JT ordering increases the number of long JT $Ni^{3+}−O$ bonds directed toward Al, accommodating the strain of the dynamic JT distortion. Proper characterization of the Al environment in the initial metal oxide structure is essential to understanding the role of Al in structural stability and surface phase reconstruction during electrochemical cycling. The techniques outlined in this

work will be used to investigate the structural changes occurring in NCA and will be the focus of a future publication.

■ ASSOCIATED CONTENT

Ⓢ Supporting Information

The Supporting Information is available free of charge on the ACS Publications website at DOI: 10.1021/acs.chemmater.6b02797.

Additional details of the NCA phase diagram, structural and NMR shift calculations, atom probe tomography experimental details and additional maps, calculated NMR spectra, 2D ^{7}Li pj-MATPASS spectra, full deconvolution of ^{27}Al NMR spectra, and static ^{27}Al NMR shifts (PDF)

■ AUTHOR INFORMATION

Corresponding Authors
*E-mail: shmeng@ucsd.edu.
*E-mail: cpg27@cam.ac.uk.

Author Contributions
The manuscript was written through contributions of all authors. All authors have given approval to the final version of the manuscript.

Notes
The authors declare no competing financial interest.

■ ACKNOWLEDGMENTS

■ REFERENCES

(1) Liu, W.; Oh, P.; Liu, X.; Lee, M.-J.; Cho, W.; Chae, S.; Kim, Y.; Cho, J. Nickel-Rich Layered Lithium Transition-Metal Oxide for High-Energy Lithium-Ion Batteries. *Angew. Chem., Int. Ed.* **2015**, *54*, 4440−4457.

(2) Goodenough, J. B.; Wickham, D. G.; Croft, W. J. Some Magnetic and Crystallographic Properties of the System $Li_x^+Ni_{1-2x}^{+2}Ni_x^{+++}O$. *J. Phys. Chem. Solids* **1958**, *5*, 107−116.

(3) Rougier, A.; Gravereau, P.; Delmas, C. Optimization of the Composition of the $Li_{1-z}Ni_{1+z}O_2$ Electrode Materials: Structural, Magnetic, and Electrochemical Studies. *J. Electrochem. Soc.* **1996**, *143*, 1168−1175.

(4) Rougier, A.; Delmas, C.; Chadwick, A. V. Non-Cooperative Jahn-Teller Effect in $LiNiO_2$: An EXAFS Study. *Solid State Commun.* **1995**, *94*, 123−127.

(5) Vernay, F.; Penc, K.; Fazekas, P.; Mila, F. Orbital Degeneracy as a Source of Frustration in $LiNiO_2$. *Phys. Rev. B: Condens. Matter Mater. Phys.* **2004**, *70*, 014428.

(6) Stoyanova, R.; Zhecheva, E.; Friebel, C. Magnetic Interactions in Layered $LiNiO_2$ Revealed by EPR of Ni^{3+}. *J. Phys. Chem. Solids* **1993**, *54*, 9−13.

(7) Delmas, C.; Saadoune, I.; Dordor, P. Effect of Cobalt Substitution on the Jahn-Teller Distortion of the $NaNiO_2$ Layered Oxide. *Mol. Cryst. Liq. Cryst. Sci. Technol., Sect. A* **1994**, *244*, 337−342.

(8) Armstrong, A. R.; Bruce, P. G. Synthesis of Layered $LiMnO_2$ as an Electrode for Rechargeable Lithium Batteries. *Nature* **1996**, *381*, 499−500.

(9) Capitaine, F.; Gravereau, P.; Delmas, C. A New Variety of $LiMnO_2$ with a Layered Structure. *Solid State Ionics* **1996**, *89*, 197−202.

(10) Stoyanova, R.; Zhecheva, E.; Alcantara, R.; Tirado, J. L. Local Coordination of Low-Spin Ni^{3+} Probes in Trigonal $LiAl_yCo_{1-y}O_2$ Monitored by HF-EPR. *J. Phys. Chem. B* **2004**, *108*, 4053−4057.

(11) Sugiyama, J.; Ikedo, Y.; Mukai, K.; Nozaki, H.; Mansson, M.; Ofer, O.; Harada, M.; Kamazawa, K.; Miyake, Y.; Brewer, J. H.; Ansaldo, E. J.; Chow, K. H.; Watanabe, I.; Ohzuku, T. Low-Temperature Magnetic Properties and High-Temperature Diffusive Behavior of $LiNiO_2$ Investigated by Muon-Spin Spectroscopy. *Phys. Rev. B: Condens. Matter Mater. Phys.* **2010**, *82*, 224412.

(12) Rougier, A.; Saadoune, I.; Gravereau, P.; Willmann, P.; Delmasa, C. Effect of Cobalt Substitution on Cationic Distribution in $LiNi_{1-y}Co_yO_2$ Electrode Materials. *Solid State Ionics* **1996**, *90*, 83−90.

(13) Conry, T. E.; Mehta, A.; Cabana, J.; Doeff, M. M. XAFS Investigations of $LiNi_{0.45}Mn_{0.45}Co_{0.1-y}Al_yO_2$ Positive Electrode Materials. *J. Electrochem. Soc.* **2012**, *159*, A1562−A1571.

(14) Conry, T. E.; Mehta, A.; Cabana, J.; Doeff, M. M. Structural Underpinnings of the Enhanced Cycling Stability upon Al-Substitution in $LiNi_{0.45}Mn_{0.45}Co_{0.1-y}Al_yO_2$ Positive Electrode Materials for Li-ion Batteries. *Chem. Mater.* **2012**, *24*, 3307−3317.

(15) Madhavi, S.; Rao, G. V. S.; Chowdari, B. V. R.; Li, S. F. Y. Effect of Aluminium Doping on Cathodic Behaviour of $LiNi_{0.7}Co_{0.3}O_2$. *J. Power Sources* **2001**, *93*, 156−162.

(16) Guilmard, M.; Croguennec, L.; Denux, D.; Delmas, C. Thermal Stability of Lithium Nickel Oxide Derivatives. Part I: $Li_xNi_{1.02}O_2$ and $Li_xNi_{0.89}Al_{0.16}O_2$ (x = 0.50 and 0.30). *Chem. Mater.* **2003**, *15*, 4476−4483.

(17) Guilmard, M.; Croguennec, L.; Delmas, C. Thermal Stability of Lithium Nickel Oxide Derivatives. Part II: $Li_xNi_{0.70}Co_{0.15}Al_{0.15}O_2$ and $Li_xNi_{0.90}Mn_{0.10}O_2$ (x = 0.50 and 0.30). Comparison with $Li_xNi_{1.02}O_2$ and $Li_xNi_{0.89}Al_{0.16}O_2$. *Chem. Mater.* **2003**, *15*, 4484−4493.

(18) Croguennec, L.; Bains, J.; Bréger, J.; Tessier, C.; Biensan, P.; Levasseur, S.; Delmas, C. Effect of Aluminum Substitution on the Structure, Electrochemical Performance and Thermal Stability of $Li_{1+x}(Ni_{0.40}Mn_{0.40}Co_{0.20-z}Al_z)_{1-x}O_2$. *J. Electrochem. Soc.* **2011**, *158*, A664−A670.

(19) Zhou, F.; Zhao, X. M.; Jiang, J. W.; Dahn, J. R. Advantages of Simultaneous Substitution of Co in $Li[Ni_{1/3}Mn_{1/3}Co_{1/3}]O_2$ by Ni and Al. *Electrochem. Solid-State Lett.* **2009**, *12*, A81−A83.

(20) Zhou, F.; Zhao, X. M.; Dahn, J. R. Synthesis, Electrochemical Properties, and Thermal Stability of Al-Doped Li-$Ni_{1/3}Mn_{1/3}Co_{(1/3-z)}Al_zO_2$ Positive Electrode Materials. *J. Electrochem. Soc.* **2009**, *156*, A343−A347.

(21) Croguennec, L.; Shao-Horn, Y.; Gloter, A.; Colliex, C.; Guilmard, M.; Fauth, F.; Delmas, C. Segregation Tendency in Layered Aluminum-Substituted Lithium Nickel Oxides. *Chem. Mater.* **2009**, *21*, 1051−1059.

(22) Devaraj, A.; Gu, M.; Colby, R.; Yan, P.; Wang, C. M.; Zheng, J. M.; Xiao, J.; Genc, A.; Zhang, J. G.; Belharouak, I.; Wang, D.; Amine, K.; Thevuthasan, S. Visualizing Nanoscale 3D Compositional Fluctuation of Lithium in Advanced Lithium-ion Battery Cathodes. *Nat. Commun.* **2015**, *6*, 8014.

(23) Grey, C. P.; Dupre, N. NMR Studies of Cathode Materials for Lithium-ion Rechargeable Batteries. *Chem. Rev.* **2004**, *104*, 4493−4512.

(24) Gaudin, E.; Taulelle, F.; Stoyanova, R.; Zhecheva, E.; Alcantara, R.; Lavela, P.; Tirado, J. L. Cobalt(III) Effect on Al-27 NMR Chemical Shifts in $LiAl_xCo_{1-x}O_2$. *J. Phys. Chem. B* **2001**, *105*, 8081−8087.

(25) Stoyanova, R.; Zhecheva, E.; Kuzmanova, E.; Alcantara, R.; Lavela, P.; Tirado, J. L. Aluminium Coordination in $LiNi_{1-y}Al_yO_2$ Solid Solutions. *Solid State Ionics* **2000**, *128*, 1−10.

(26) Lee, Y.; Woo, A. J.; Han, K.-S.; Ryu, K. S.; Sohn, D.; Kim, D.; Lee, H. Solid-state NMR Studies of Al-doped and Al_2O_3-coated $LiCoO_2$. *Electrochim. Acta* **2004**, *50*, 491−494.

(27) Rosina, K. J.; Jiang, M.; Zeng, D. L.; Salager, E.; Best, A. S.; Grey, C. P. Structure of Aluminum Fluoride Coated Li-$[Li_{1/9}Ni_{1/3}Mn_{5/9}]O_2$ Cathodes for Secondary Lithium-ion Batteries. *J. Mater. Chem.* **2012**, *22*, 20602−20610.

(28) Alcántara, R.; Lavela, P.; Relaño, P. L.; Tirado, J. L.; Zhecheva, E.; Stoyanova, R. X-ray Diffraction, EPR, and ^6Li and ^{27}Al MAS NMR Study of $LiAlO_2$−$LiCoO_2$ Solid Solutions. *Inorg. Chem.* **1998**, *37*, 264−269.

(29) Clément, R. J.; Pell, A. J.; Middlemiss, D. S.; Strobridge, F. C.; Miller, J. K.; Whittingham, M. S.; Emsley, L.; Grey, C. P.; Pintacuda, G. Spin-Transfer Pathways in Paramagnetic Lithium Transition-Metal Phosphates from Combined Broadband Isotropic Solid-State MAS NMR Spectroscopy and DFT Calculations. *J. Am. Chem. Soc.* **2012**, *134*, 17178−17185.

(30) Wilkening, M.; Romanova, E. E.; Nakhal, S.; Weber, D.; Lerch, M.; Heitjans, P. Time-Resolved and Site-Specific Insights into Migration Pathways of Li^+ in α-Li_3VF_6 by ^6Li 2D Exchange MAS NMR. *J. Phys. Chem. C* **2010**, *114*, 19083−19088.

(31) Marichal, C.; Hirschinger, J.; Granger, P.; Menetrier, M.; Rougier, A.; Delmas, C. ^6Li and ^7Li NMR in the $LiNi_{1-y}Co_yO_2$ Solid Solution $(0 \leq y \leq 1)$. *Inorg. Chem.* **1995**, *34*, 1773−1778.

(32) Dupre, N.; Cuisinier, M.; Martin, J. F.; Guyomard, D. Interphase Evolution at Two Promising Electrode Materials for Li-Ion Batteries: $LiFePO_4$ and $LiNi_{1/2}Mn_{1/2}O_2$. *ChemPhysChem* **2014**, *15*, 1922−1938.

(33) Carlier, D.; Menetrier, M.; Grey, C. P.; Delmas, C.; Ceder, G. Understanding the NMR Shifts in Paramagnetic Transition Metal Oxides Using Density Functional Theory Calculations. *Phys. Rev. B: Condens. Matter Mater. Phys.* **2003**, *67*, 174103.

(34) Middlemiss, D. S.; Ilott, A. J.; Clément, R. J.; Strobridge, F. C.; Grey, C. P. Density Functional Theory-Based Bond Pathway Decompositions of Hyperfine Shifts: Equipping Solid-State NMR to Characterize Atomic Environments in Paramagnetic Materials. *Chem. Mater.* **2013**, *25*, 1723−1734.

(35) Britto, S.; Leskes, M.; Hua, X.; Hebert, C. A.; Shin, H. S.; Clarke, S.; Borkiewicz, O.; Chapman, K. W.; Seshadri, R.; Cho, J.; Grey, C. P. Multiple Redox Modes in the Reversible Lithiation of High-Capacity, Peierls-Distorted Vanadium Sulfide. *J. Am. Chem. Soc.* **2015**, *137*, 8499−8508.

(36) Durupthy, O.; Maquet, J.; Bonhomme, C.; Coradin, T.; Livage, J.; Steunou, N. Room Temperature Sol-Gel Synthesis of Crystalline $Cs[V_3O_8]$. Probing the Hydration Level of the Interlamellar Space by ^{51}V and ^{133}Cs MAS NMR Spectroscopy. *J. Mater. Chem.* **2008**, *18*, 3702−3712.

(37) Dupre, N.; Gaubicher, J.; Guyomard, D.; Grey, C. P. ^7Li and ^{51}V MAS NMR Study of the Electrochemical Behavior of $Li_{1-x}V_3O_8$. *Chem. Mater.* **2004**, *16*, 2725−2733.

(38) Stallworth, P. E.; Guo, X.; Tatham, E.; Greenbaum, S. G.; Arrabito, M.; Bodoarado, S.; Penazzi, N. A solid-state ^{51}V NMR characterization of vanadium sites in $LiCo_xNi_{1-x}VO_4$. *Solid State Ionics* **2004**, *170*, 181−186.

(39) Stallworth, P. E.; Johnson, F. S.; Greenbaum, S. G.; Passerini, S.; Flowers, J.; Smyrl, W. Magnetic Resonance Studies of Chemically Intercalacted $Li_xV_2O_5$ Aerogels. *J. Appl. Phys.* **2002**, *92*, 3839−3852.

(40) Hung, I.; Zhou, L.; Pourpoint, F.; Grey, C. P.; Gan, Z. Isotropic High Field NMR Spectra of Li-Ion Battery Materials with Anisotropy > 1 MHz. *J. Am. Chem. Soc.* **2012**, *134*, 1898−1901.

(41) Kim, J.; Middlemiss, D. S.; Chernova, N. A.; Zhu, B. Y. X.; Masquelier, C.; Grey, C. P. Linking Local Environments and Hyperfine Shifts: A Combined Experimental and Theoretical ^{31}P and ^7Li Solid-State NMR Study of Paramagnetic Fe(III) Phosphates. *J. Am. Chem. Soc.* **2010**, *132*, 16825−16840.

(42) Dogan, F.; Vaughey, J. T.; Iddir, H.; Key, B. Direct Observation of Lattice Aluminum Environments in Li Ion Cathodes $LiNi_{1-y-z}Co_yAl_zO_2$ and Al-Doped $LiNi_xMn_yCo_zO_2$ via ^{27}Al MAS NMR Spectroscopy. *ACS Appl. Mater. Interfaces* **2016**, *8*, 16708−16717.

(43) Larson, A. C.; Dreele, R. B. V. *General Structure Analysis System (GSAS)*; Report LAUR 86-748; Los Alamos National Laboratory: 2004.

(44) Toby, B. H.; EXPGUI, A. Graphical User Interface for GSAS. *J. Appl. Crystallogr.* **2001**, *34*, 210−213.

(45) Kresse, G.; Hafner, J. Ab Initio Molecular-Dynamics for Liquid-Metals. *Phys. Rev. B: Condens. Matter Mater. Phys.* **1993**, *47*, 558−561.

(46) Kresse, G.; Hafner, J. Ab-Initio Molecular-Dynamics Simluation of the Liquid-Metal Amorphous-Semiconductor Transition in Germanium. *Phys. Rev. B: Condens. Matter Mater. Phys.* **1994**, *49*, 14251−14269.

(47) Kresse, G.; Furthmuller, J. Efficiency of Ab-Initio Total Energy Calculations for Metals and Semiconductors Using a Plane-Wave Basis Set. *Comput. Mater. Sci.* **1996**, *6*, 15−50.

(48) Kresse, G.; Furthmuller, J. Efficient Iterative Schemes for Ab Initio Total-Energy Calculations Using a Plane-Wave Basis Set. *Phys. Rev. B: Condens. Matter Mater. Phys.* **1996**, *54*, 11169−11186.

(49) Dudarev, S. L.; Botton, G. A.; Savrasov, S. Y.; Humphreys, C. J.; Sutton, A. P. Electron-Energy-Loss Spectra and the Structural Stability of Nickel Oxide: An LSDA+U Study. *Phys. Rev. B: Condens. Matter Mater. Phys.* **1998**, *57*, 1505−1509.

(50) Blochl, P. E. Projector Augmented-Wave Method. *Phys. Rev. B: Condens. Matter Mater. Phys.* **1994**, *50*, 17953−17979.

(51) Kresse, G.; Joubert, D. From Ultrasoft Pseudopotentials to the Projector Augmented-Wave Method. *Phys. Rev. B: Condens. Matter Mater. Phys.* **1999**, *59*, 1758−1775.

(52) Thomas, J. C.; Puchala, B.; Goiri, J.; Natarajan, A.; Chen, M.-H.; Bechtel, J.; Radin, M. D.; Decolvenaere, E.; Belak, A.; Van der Ven, A. *CASM, v0.1.0*; 2015. Available from https://github.com/prisms-center/CASMcode. DOI: 10.5281/zenodo.31216.

(53) Thomas, J. C.; Van der Ven, A. Finite-Temperature Properties of Strongly Anharmonic and Mechanically Unstable Crystal Phases from First Principles. *Phys. Rev. B: Condens. Matter Mater. Phys.* **2013**, *88*, 214111.

(54) Puchala, B.; Van der Ven, A. Thermodynamics of the Zr-O System from First-Principles Calculations. *Phys. Rev. B: Condens. Matter Mater. Phys.* **2013**, *88*, 094108.

(55) Van der Ven, A.; Thomas, J. C.; Xu, Q.; Bhattacharya, J. Linking the Electronic Structure of Solids to their Thermodynamic and Kinetic Properties. *Math. Comput. Simul.* **2010**, *80*, 1393−1410.

(56) Buta, S.; Morgan, D.; Van der Ven, A.; Aydinol, M. K.; Ceder, G. Phase Separation Tendencies of Aluminum-Doped Transition-Metal Oxides ($LiAl_{1-x} M_x O_2$) in the α-$NaFeO_2$ Crystal Structure. *J. Electrochem. Soc.* **1999**, *146*, 4335−4338.

(57) Kim, J.; Ilott, A. J.; Middlemiss, D. S.; Chernova, N. A.; Pinney, N.; Morgan, D.; Grey, C. P. ^2H and ^{27}Al Solid-State NMR Study of the Local Environments in Al-Doped 2-Line Ferrihydrite, Goethite, and Lepidocrocite. *Chem. Mater.* **2015**, *27*, 3966−3978.

(58) Dovesi, R.; Saunders, V. R.; Roetti, C.; Orlando, R.; Zicovich-Wilson, C. M.; Pascale, F.; Civalleri, B.; Doll, K.; Harrison, N. M.; Bush, I. J.; D'Arco, P.; Llunell, M. *CRYSTAL09 User's Manual*; University of Torino: Torino, 2009.

(59) Zhang, Y.; Castets, A.; Carlier, D.; Ménétrier, M.; Boucher, F. Simulation of NMR Fermi Contact Shifts for Lithium Battery Materials: The Need for an Efficient Hybrid Functional Approach. *J. Phys. Chem. C* **2012**, *116*, 17393−17402.

(60) Becke, A. D. Density-Functional Thermochemistry. III. The Role of Exact Exchange. *J. Chem. Phys.* **1993**, *98*, 5648−5652.

(61) Lee, C.; Yang, W.; Parr, R. G. Development of the Colle-Salvetti Correlation-Energy Formula into a Functional of the Electron Density. *Phys. Rev. B: Condens. Matter Mater. Phys.* **1988**, *37*, 785−789.

(62) Schäfer, A.; Horn, H.; Ahlrichs, R. Fully Optimized Contracted Gaussian Basis Sets for Atoms Li to Kr. *J. Chem. Phys.* **1992**, *97*, 2571−2577.

(63) Kutzelnigg, W.; Fleischer, U.; Schindler, M. The IGLO-Method: Ab-initio Calculation and Interpretation of NMR Chemical Shifts and Magnetic Susceptibilities. In *NMR Basic Principles and Progress*; Springer Berlin Heidelberg: Berlin, Heidelberg, 1991; Vol. 23, pp 165−262.

(64) Liu, H. D.; Xu, J.; Ma, C. Z.; Meng, Y. S. A New O3-type Layered Oxide Cathode with High Energy/Power Density for Rechargeable Na Batteries. *Chem. Commun.* **2015**, *51*, 4693−4696.

(65) Liu, H.; Fell, C. R.; An, K.; Cai, L.; Meng, Y. S. In-situ Neutron Diffraction Study of the $xLi_2MnO_3 \cdot (1 - x)LiMO_2$ ($x = 0, 0.5$; M = Ni, Mn, Co) Layered Oxide Compounds During Electrochemical Cycling. *J. Power Sources* **2013**, *240*, 772−778.

(66) Liu, H. D.; Qian, D. N.; Verde, M. G.; Zhang, M. H.; Baggetto, L.; An, K.; Chen, Y.; Carroll, K. J.; Lau, D.; Chi, M. F.; Veith, G. M.; Meng, Y. S. Understanding the Role of NH_4F and Al_2O_3 Surface Co-modification on Lithium-Excess Layered Oxide $Li_{1.2}Ni_{0.2}Mn_{0.6}O_2$. *ACS Appl. Mater. Interfaces* **2015**, *7*, 19189−19200.

(67) Murakami, M.; Shimoda, K.; Ukyo, Y.; Arai, H.; Uchimoto, Y.; Ogumi, Z. ^{7}Li NMR Study on Irreversible Capacity of Li-$Ni_{0.8-x}Co_{0.15}Al_{0.05}Mg_xO_2$ Electrode in a Lithium-Ion Battery. *J. Electrochem. Soc.* **2015**, *162*, A1315−A1318.

(68) Chen, H.; Dawson, J. A.; Harding, J. H. Effects of Cationic Substitution on Structural Defects in Layered Cathode Materials $LiNiO_2$. *J. Mater. Chem. A* **2014**, *2*, 7988−7996.